Fractal Electrochemical Microsupercapacitors

Mrinal K. Hota, Qiu Jiang, Yousof Mashraei, Khaled N. Salama,* and Husam N. Alshareef*

The first successful fabrication of microsupercapacitors (μ-SCs) using fractal electrode designs is reported. Using sputtered anhydrous RuO_2 thin-film electrodes as prototypes, μ-SCs are fabricated using Hilbert, Peano, and Moore fractal designs, and their performance is compared to conventional interdigital electrode structures. Microsupercapacitor performance, including energy density, areal and volumetric capacitances, changes with fractal electrode geometry. Specifically, the μ-SCs based on the Moore design show a 32% enhancement in energy density compared to conventional interdigital structures, when compared at the same power density and using the same thin-film RuO_2 electrodes. The energy density of the Moore design is 23.2 mWh cm^{-3} at a volumetric power density of 769 mW cm^{-3}. In contrast, the interdigital design shows an energy density of only 17.5 mWh cm^{-3} at the same power density. We show that active electrode surface area cannot alone explain the increase in capacitance and energy density. We propose that the increase in electrical lines of force, due to edging effects in the fractal electrodes, also contribute to the higher capacitance. This study shows that electrode fractal design is a viable strategy for improving the performance of integrated μ-SCs that use thin-film electrodes at no extra processing or fabrication cost.

1. Introduction

There is currently an increasing demand for small and autonomous electronic devices—such as wearable sensors, implantable medical devices, and microrobots—all of which require compact and efficient energy-storage solutions.[1,2] Thin-film and 3D microbatteries have been proposed as solutions, but they often suffer from a poor rate performance and a short cycle life.[3] In contrast, μ-SCs are promising for such applications because of their charge–discharge (CD) rate, high power density, and long cycle life.[4] In addition, compared to thin-film batteries, μ-SCs charge most efficiently by drawing the maximum current that the source can supply, irrespective of voltage, thereby making supercapacitors more appropriate

for self-powered system applications in which the generated voltage may be intermittent.[5] Supercapacitors come in two main types according to their charge-storage mechanism: electric double-layer capacitors (EDLCs) and pseudocapacitors.[6] EDLCs store energy through the accumulation (adsorption) of charges on the surface of the electrode material. In contrast, pseudocapacitors store charges mainly through faradaic reactions.[7] The EDLCs are usually characterized by a high power density, while pseudocapacitors are known to have higher energy densities than EDLCs.[8] The recent trend in the supercapacitor or electrochemical capacitor research is to develop μ-SCs that are compatible with Si-integrated circuits (ICs).[9] Carbon-based materials have been used widely as an active electrode material for the development of μ-SCs devices. However, the integration of carbon-based materials in Si-based ICs is relatively challenging.[10] To solve this technological bottleneck, Si IC-compatible materials that can be deposited using microfabrication compatible methods (e.g., sputtering, atomic layer deposition, evaporation) are preferred. Several transition metal oxides—such as Co_3O_4, MnO_2, NiO, and RuO_2—are widely used as active electrode material in μ-SC research.[11–14] The processes used to prepare these oxides can have a marked influence on electrode performance in supercapacitor devices.[15] For example, it is well known that, due to their porous structure and large surface area, chemically prepared nanostructured oxides can offer more capacitance than vacuum-deposited thin films.[16,17] However, these chemical processes may not provide the best approach to the fabrication of integrated μ-SCs, especially if these μ-SCs are to be interfaced with other electronic devices. Hence, vacuum-deposited supercapacitive materials (e.g., sputtered)—which can be more amenable to the fabrication of μ-SCs—are preferred despite their lower capacitance compared to chemically prepared materials.

One way to improve the performance of μ-SCs that use vacuum-deposited thin films is through electrode design. Thus, this paper explores fractal electrode designs as a means to improve the performance of integrated μ-SCs. The fractal concept applies to any object whose form is extremely irregular and/or fragmented at all scales.[18,19] Various types of fractal topologies are available—from lines to loops—that can be tailored for specific electronic applications. A fractal design is generally prepared using an algorithm with a finite number of iterations by starting from an initial structure or unit-cell design (called a "generator") that is replicated many times at different scales, positions, and directions to cultivate the final fractal

Dr. M. K. Hota, Q. Jiang, Y. Mashraei, Prof. K. N. Salama,
Prof. H. N. Alshareef
Physical Sciences and Engineering Division
King Abdullah University of Science and Technology (KAUST)
Thuwal 23955-6900, Saudi Arabia
E-mail: khaled.salama@kaust.edu.sa; husam.alshareef@kaust.edu.sa
Y. Mashraei, Prof. K. N. Salama
Computer, Electrical and Mathematical Sciences
and Engineering Division
King Abdullah University of Science and Technology (KAUST)
Thuwal 23955-6900, Saudi Arabia

The ORCID identification number(s) for the author(s) of this article can be found under https://doi.org/10.1002/aelm.201700185.

DOI: 10.1002/aelm.201700185

**ADVANCED
SCIENCE NEWS**
www.advancedsciencenews.com

**ADVANCED
ELECTRONIC
MATERIALS**
www.advelectronicmat.de

structure.[20,21] Given the potential advantages of fractal designs, many research groups have recently started to work on fractal electrode designs for several applications, such as in characterization of complex irregular surfaces,[22] neural stimulation,[23] high-density CMOS capacitors,[24] optoelectronic devices,[25,26] biosensors,[27] stretchable electronics,[28] and in radio frequency (RF) MEMS capacitors.[21,29] Fractal designs have also been theoretically predicted to enhance the performance of electrochemical systems since they maximize the electrochemically active surface area while minimizing energy lost during the transport of ions within the fractal network.[30] A relatively large surface area can be achieved in the case of fractal designs, which may result in an overall increase of volumetric capacitance.[31]

Here, we fabricated µ-SCs using three different fractal-electrode designs, and we compared their performance to conventional interdigital structures. The specific fractal designs that we used are fractal Hilbert (FH),[32] fractal Moore (FM),[33] and Peano.[34] Radio frequency, reactive sputter-deposited RuO₂ thin films were used as active electrode material. Though hydrous RuO₂ prepared by chemical methods may offer a better electrochemical performance, sputtered RuO₂ was used due to its excellent uniform thickness over a wide area; such uniformity facilitates the integration of the fractal µ-SCs with other electronic components. The main purpose of this study is to demonstrate fractal electrode designs for µ-SC applications and to compare their performance with conventional, interdigitated electrode designs.

2. Results and Discussion

2.1. Material Characterizations

Figure 1a shows the X-ray diffraction (XRD) patterns obtained from pure Ru thin films and from RuO_2 films deposited with different oxygen partial pressure (O_{pp}) at room temperature. It can be seen from the XRD patterns that all RuO_2 films are polycrystalline. Moreover, the number of crystalline peaks increases with increasing O_{pp}. Major characteristic diffraction peaks—which are identified as (110) at $2\theta = 28.2°$, (101) at $2\theta = 33.3°$, (200) at $2\theta = 40.33°$, and (210) at $2\theta = 48.01°$—are consistent with the rutile crystal structure of RuO_2.[35,36] The sharp, crystalline peaks signify the absence of hydroxyl groups in these films, which is expected when using a sputtering process.[37,38] The chemical composition of different RuO_2 films was also characterized by Raman spectroscopy, as shown in Figure 1b. It can be clearly observed that the RuO_2 films deposited with more than 15% O_{pp} exhibit first-order phonon bands of the rutile RuO_2 structure, as seen from the three major peaks indexed at 509, 630, and 695 cm^{-1}, which are related to E_g, A_{1g}, and B_{2g}, respectively.[39] It is found that all the three major features show a blue shift of the peak location.[40] The chemical compositions of the reactively sputtered RuO_2 films were analyzed using high-resolution X-ray photoelectron spectroscopy (XPS). All XPS spectra were deconvoluted using the standard Gaussian–Lorentzian function after background correction by
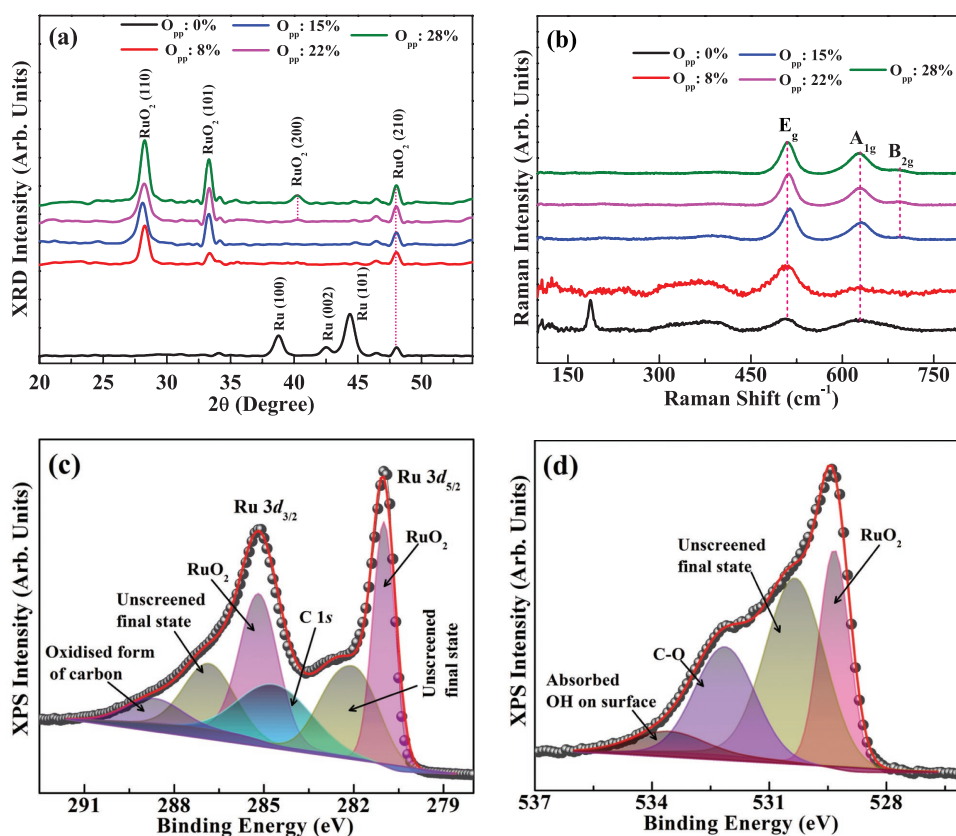

Figure 1. Material characterizations of RF sputter-deposited RuO_2 films. a) The XRD diffraction patterns and b) Raman spectra obtained from RuO_2 films deposited with different O_{pp}. The XPS core level spectra of c) Ru 3d and d) O 1s obtained from 28% O_{pp} RuO_2 films.

**ADVANCED
SCIENCE NEWS**
www.advancedsciencenews.com

**ADVANCED
ELECTRONIC
MATERIALS**
www.advelectronicmat.de

the Shirley method. It was found that XPS spectra obtained for Ru 3d shift toward higher binding energy with increasing oxygen partial pressure, as shown in Figure S1 (Supporting Information). Figure 1c shows the XPS spectra obtained from Ru 3d, which has a 5/2 and 3/2 spin–orbit doublet shape. Two relatively narrow doublet peaks at 281.0 and 285.2 eV with a spin–orbit separation of 4.2 eV originate from RuO_2.[41] There is also another doublet at higher energy at 282.1 and 286.84 eV, which may be due to a higher oxidation state of Ru. The relatively low binding energy spin–orbit doublet of RuO_2 may be due to the screened final-state effect. On the other hand, the spin–orbit doublet at higher binding energy may be due to the unscreened final state. The peak at 284.6 eV is related to carbon surface contamination. A small peak at 288.68 eV may be due to an oxidized form of carbon, such as carbonate. These results of Ru 3d are similar to previously reported XPS studies of anhydrous RuO_2, which is also the case for our sputtered RuO_2 films.[42] The O 1s spectra obtained from the 28% O_{pp} RuO_2 sample is shown in Figure 1d. Note that the O 1s spectrum has four components. The peak at 529.35 eV with a relatively narrow FWHM (full width at half maximum) is attributed to O^{2-} (oxygen bound to Ru).[43] This component has a slightly asymmetric tail on the high binding energy side, which is due to the screening effect. The relatively broad peak at 530.34 eV is primarily due to the many-body screening effect of the conduction electrons and is related to the unscreened final-state effect of Ru.[44] The peak at the higher binding energy of 532.13 eV indicates the presence of oxygen-containing carbon bonds that are assigned to organic C−O bonds.[45] Another small peak at 533.6 eV, which contains only 5.8% of the total area, belongs to absorbed water on the surface of the RuO_2 films.[46] The absorption of water by a hygroscopic oxide such as RuO_2 is common, especially when it is exposed to the ambient. Hence, from the XRD and XPS results, it is clear that the RuO_2 films deposited by reactive sputtering are anhydrous. Top-view images of actual μ-SCs devices obtained by 3D surface profiler imaging (NewView 7300, Zygo) are shown in **Figure 2**a–d for IDE, FH, Peano, and FM electrode designs, respectively. All designs use 100 µm wide electrodes and a 50 µm interelectrode spacing on a glass substrate. The deposited RuO_2 films are uniform for all devices.

2.2. Electrochemical Characterizations

We have characterized the electrochemical properties of our devices using cyclic voltammograms (CV) and galvanostatic CD methods. The electrochemical reaction at the sputter-deposited, anhydrous RuO_2 surface in the aqueous electrolyte can be described as follows
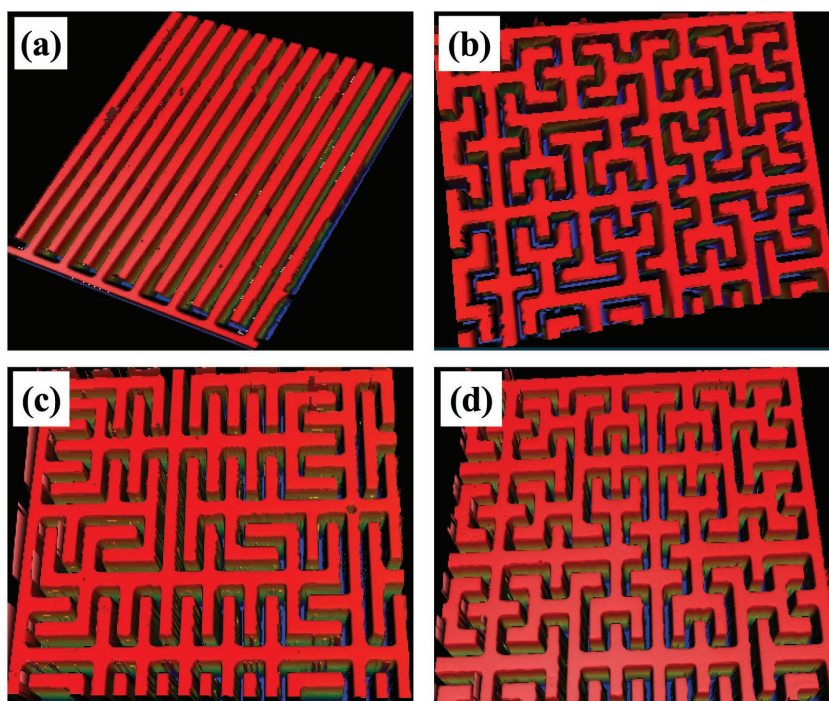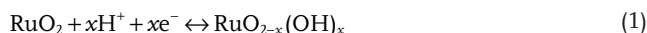

Figure 2. 3D images corresponding to a) IDE, b) FH, c) Peano, and d) FM electrode designs captured with a surface profiler (NewView 7300, Zygo).

$$RuO_2 + xH^+ + xe^- \leftrightarrow RuO_{2-x}(OH)_x \qquad (1)$$

Reversible electron transfer and the electroadsorption of protons on the RuO_2 surface contribute to its capacitive behavior.[47] The electrochemical properties of different μ-SC devices have been characterized using a two-electrode configuration with a 1 M H_2SO_4 aqueous electrolyte. To optimize the thickness of RuO_2 films for capacitive performance, we fabricated different μ-SCs, using an IDE electrode design, with 28% O_{pp} RuO_2 films of different thickness. The areal capacitance for different devices was calculated from galvanostatic charge and discharge curves measured using a current density of 0.1 mA cm^{-2}. We found that the areal capacitance increases almost linearly with the thickness of the RuO_2 film, as shown in Figure S2 (Supporting Information). However, we also found that the RuO_2 films peel off from the current collector surface after few cycles for the devices with ~900 nm of RuO_2 film. Based on these results, we used a RuO_2 thickness of ≈650 nm for the rest of the study.

Figure 3a–d shows CVs recorded at scan rates that range from 50 to 1000 mVs^{-1}, as measured with IDE, FH, Peano, and FM electrode designs, respectively. All μ-SCs exhibit excellent rectangular CV characteristics and operate within a voltage window of 1 V. The nearly rectangular CV shapes and lack of oxidation and reduction peaks are observed for all scan rates, and they indicate behavior like that of electrochemical double-layer capacitors (EDLC) for these electrodes. The origin of EDLC-type CVs in our RuO_2 electrode devices is attributed to the fast, reversible, and successive surface redox reactions of RuO_2 films.[48,49] Moreover, the CV curves show no sudden rise in current at higher potentials, which signifies that no oxygen

**ADVANCED
SCIENCE NEWS**
www.advancedsciencenews.com

**ADVANCED
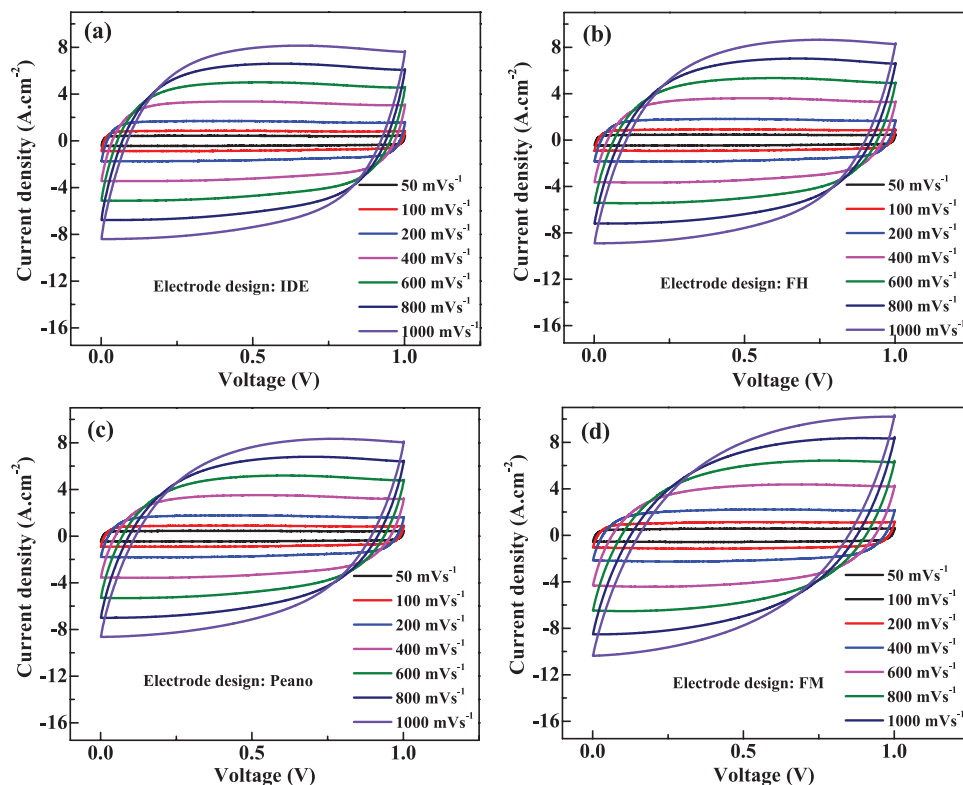ELECTRONIC
MATERIALS**
www.advelectronicmat.de

Figure 3. Electrochemical cyclic voltammograms (CVs) of different μ-SCs. Area-normalized CV curves scanned in the range of 50–1000 mV s^{-1} are shown for the μ-SCs based on a) IDE, b) FH, c) Peano, and d) FM electrode designs.

evolution occurs. However, the CV curves become less square (become lens-shaped) with increasing scan rate. The CV curves of these fabricated devices exhibit an acceptable rectangularity up to a high scan rate of 1000 mV s^{-1}. It is observed that the current density is higher in the case of fractal designs as compared to the conventional IDE-based μ-SC devices. A comparison of CV curves obtained from μ-SCs scanned at 100 mV s^{-1} is shown in Figure S3 (Supporting Information). The area under the CV curve increases in the case of the fractal electrode design as compared to IDE electrode design. This indicates that the fractal designs show a better CV performance.

The areal capacitances for different μ-SCs were calculated from the galvanostatic charge and discharge curves with an operation voltage window of 1 V. **Figure 4** shows that the charge–discharge curves obtained from different μ-SC devices show triangular-shaped curves with no obvious voltage drop at different applied current densities. Even at a very high current density (such as 3 mA cm^{-2}), the voltage drop observed from the CD curve is still negligible, which indicates a low value of equivalent series resistance. It is also found that all μ-SCs devices show nearly linear and symmetric charge–discharge curves, which suggests excellent capacitive performance and high rate capability. Figure S4 (Supporting Information) compares CD curves under the application of 0.1 mA cm^{-2} current density obtained from different electrode designs. Note that the discharge time increases in the case of the fractal electrode designs as compared to the IDE electrode design. The areal capacitance was calculated from the charge–discharge curve

as discussed in the Supporting Information file. **Figure 5**a shows the areal capacitances obtained from different electrode designs. It is found that the areal capacitance value decreases with increasing applied current density. It can also be clearly seen that the areal capacitance for the fractal designs is higher than conventional IDE designs. A maximum areal capacitance of ≈11 mF cm^{-2} was obtained from the FM electrode design, whereas ≈8 mF cm^{-2} was obtained from the IDE electrode design for the same applied current density. Moreover, a high volumetric capacitance of ≈168 F cm^{-3} was obtained from the FM electrode design, as shown in Figure 5b. The capacitance values obtained from our devices are small compared to several reports on RuO$_2$-based μ-SCs. It is well known that electrochemical capacitive behavior depends on the pore size of the active material and, in the case of RuO$_2$, on the presence of OH$^-$ molecules. However, atomic force microscopy imaging of RuO$_2$ films (see Figure S5, Supporting Information) shows that the surface of the sputtered deposited RuO$_2$ is fairly dense. In addition, our reactively sputtered RuO$_2$ films are free from OH$^-$ molecules, as XRD and XPS analyses confirm. It is worth mentioning that RuO$_2$ deposition by hydrothermal or electrodeposition process can certainly give higher capacitance.[50]

Figure 5c shows an area-normalized Ragone plot to compare the energy and power density of our μ-SC devices. It can be seen from the Ragone plot that the FM electrode can deliver a maximum volumetric energy density of 23.2 mWh cm^{-3} at a volumetric power density of 769 mW cm^{-3}. A maximum power density of 23.08 W cm^{-3} was obtained
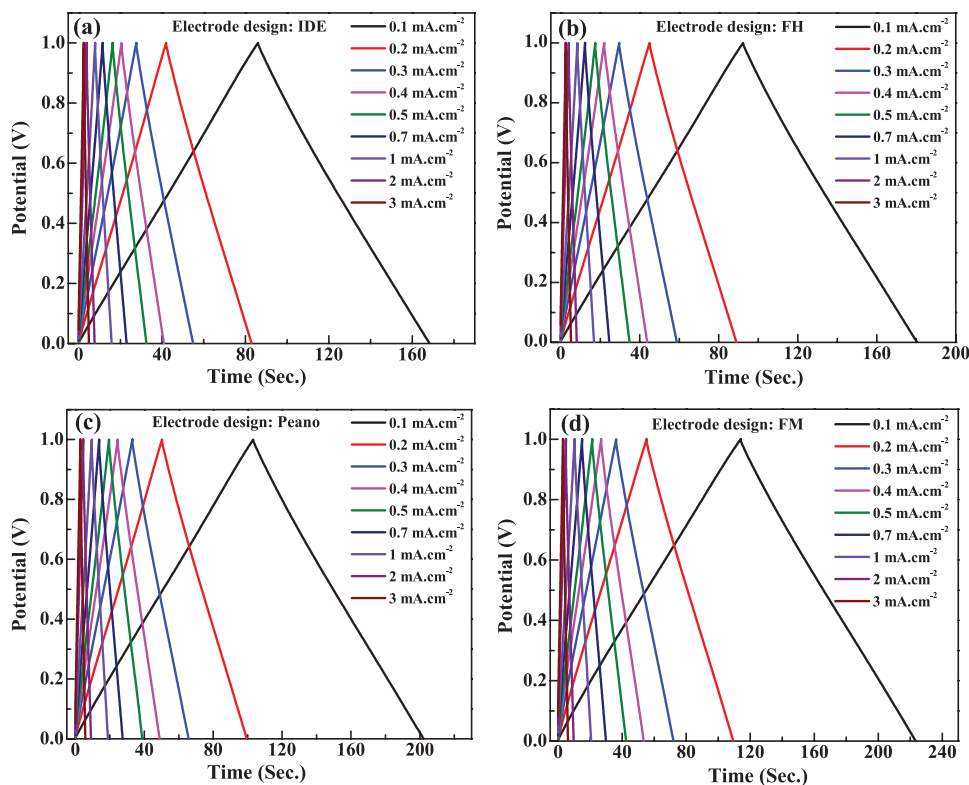
ADVANCED
SCIENCE NEWS
www.advancedsciencenews.com

ADVANCED
ELECTRONIC
MATERIALS
www.advelectronicmat.de

Figure 4. Galvanostatic charge/discharge curves measured at a current density ranging from 0.1 to 3 mA cm^{-2} for a) IDE, b) FH, c) Peano, and d) FM electrode μ-SCs.

even at an energy density of 19.38 mWh cm^{-3} from devices that use the FM fractal-electrode design. In comparison, μ-SCs based on the IDE electrode design exhibit an energy density of 15.55 mWh cm^{-3} at a similar power density (23.08 W cm^{-3}). It is worth noting that all μ-SC devices exhibit a slow drop in energy density while increasing the power density. The FM-electrode design exhibit only a small amount of energy ($\approx$16 %) loss over a wide range of power densities. The most important message in Figure 5c is that the volumetric energy density increases in the case of fractal electrode designs as compared to conventional IDE electrodes when the same electrode material is used. Specifically, an almost 32% improvement in volumetric energy density is obtained using fractal FM electrode design, as compared to IDE designs at the same power density (769 mW cm^{-3}). These results clearly demonstrate that fractal electrode designs can improve μ-SC device performance. The electrochemical impedance spectroscopy (EIS) was performed to assess the internal resistance of the μ-SCs devices. The frequency range was set to be 0.1 Hz to 1 MHz with an alternating current amplitude of 5 mV. The Nyquist plots obtained via EIS for different electrode designs are shown in Figure S6 (Supporting Information). The equivalent series resistance (ESR) values obtained from different μ-SCs devices are found to vary between 24 and 34 Ω. The relatively high resistance may be due to the relatively low ionic mobility within the dense, pore-free sputtered RuO$_2$ electrodes.[51,52]

The long-term cyclic stability of μ-SC devices using the FM electrode design was evaluated by continuous charging and

discharging over 10 000 cycles at 1 mA cm^{-2} current density, as shown in Figure 5d. Nearly 90% of the initial capacitance was retained after 10 000 cycles with almost 100% Coulombic efficiency. After the μ-SCs with FM electrode design were charged to 1 V, as shown in the inset of Figure 5d, we monitored the self-discharging process. The inset shows that the device holds about 40% of initial voltage even after 2.5 h. Hence, a decay rate of $\approx$0.24 V h^{-1} was observed, which is reasonable for aqueous electrolytic media. Electrical double-layer supercapacitors deliver quite rapid ion adsorption and desorption in double layers at the interface between materials and electrolyte, thereby leading to the inevitable voltage decrease with time in μ-SCs. Although a relatively rapid decrease of voltage was observed, these times may be sufficient for many applications that require energy for only tens of seconds. This includes wearable and implantable medical sensors that intermittently measure and transmit signals.

It is important to understand why fractal electrode designs appear to improve μ-SC device performance over conventional IDE electrode designs. It is well known that electrical field lines of force increase for edge-intensive electrodes as compared to continuous or round-shape electrode designs. Due to this edging mechanism, IDE electrode designs show better capacitance performance compared to parallel plate capacitors due to increased lateral electrical flux.[21,31] This is one of the reasons why IDE design has been the dominant electrode design in μ-SC studies. However, in the case of fractal designs, the lateral electrical flux due to the edging effects can be enhanced as compared to IDE
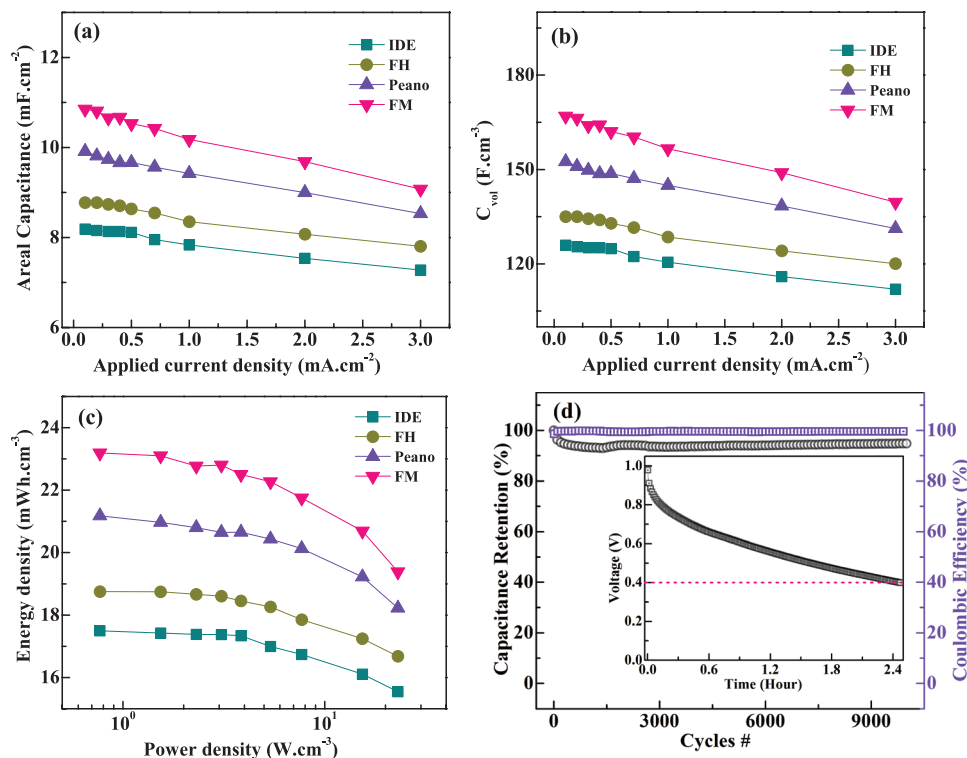
Figure 5. a) The variation of areal capacitance and b) volumetric capacitance with the applied current density. c) Ragone plot showing the energy and power density of different electrode designs. d) The capacitive retention and Coulombic efficiency versus cycle number measured at an applied current density of 1 mA cm⁻² from FM electrode designs. Inset shows the self-discharge performance of FM μ-SC.
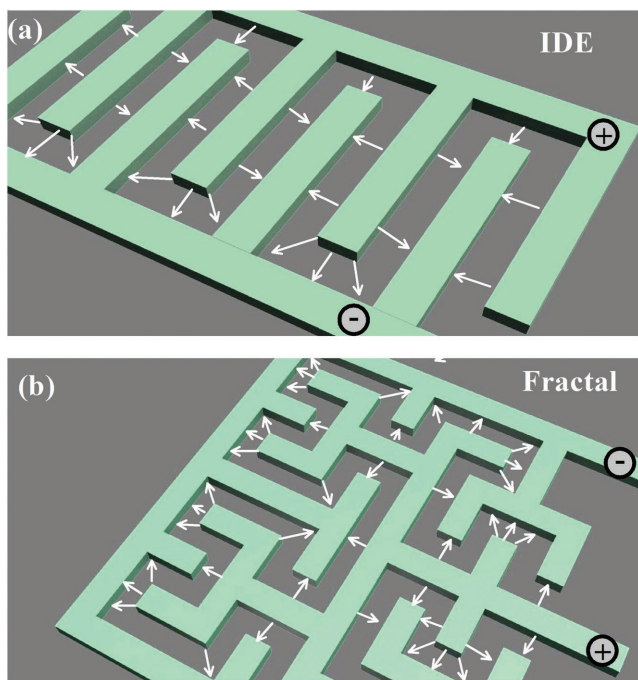

Figure 6. A schematic illustration of the edging effect in a) conventional IDE and b) fractal electrode designs. Number of electrical lines of force increases in the case of fractal electrodes due to the edging effect, originating from the existence of several open-edge segments.

designs. For a given unit area, the number of open edges in fractal designs is higher than in IDE or parallel plate designs.[24] As a result of this edging effect, electrical lines of force are more abundant in the case of fractal electrode designs, as illustrated in **Figure 6**. As a result of the increase in the electrical lines of force in fractal designs, charge (electrolyte ions) accumulation on or near the electrodes will be greater, which leads to enhanced capacitance. However, the number of open edges in the fractal electrode design depends on its order number. For the same type of fractal design, the number of edges increases with increasing order of the fractal. Also, different fractal designs have different geometry and, hence, a different number of open edges. However, it is well-known that the electrochemical performance of a μ-SC device also depends on the surface area of the active electrode material.[4,53] For fractal electrodes, the total active surface area of the device is proportional to the number of the smallest elements in a fractal design.[30] A comparison of the electroactive surface area, volume, and perimeter to area ratio for different designs is shown in Figure S7 (Supporting Information). It can be seen that the difference in the active electrode surface area and volume between the IDE design and fractal designs (FH, FP, FM) is less than 18%. However, as shown in Figure 5, the FM design has 32% higher capacitance than the IDE design. Thus, we can conclude that besides surface area of the exposed active material, there should be an additional mechanism which causes capacitance variations among the different designs. The electrical field distribution in the conventional IDE and one fractal electrode design are shown
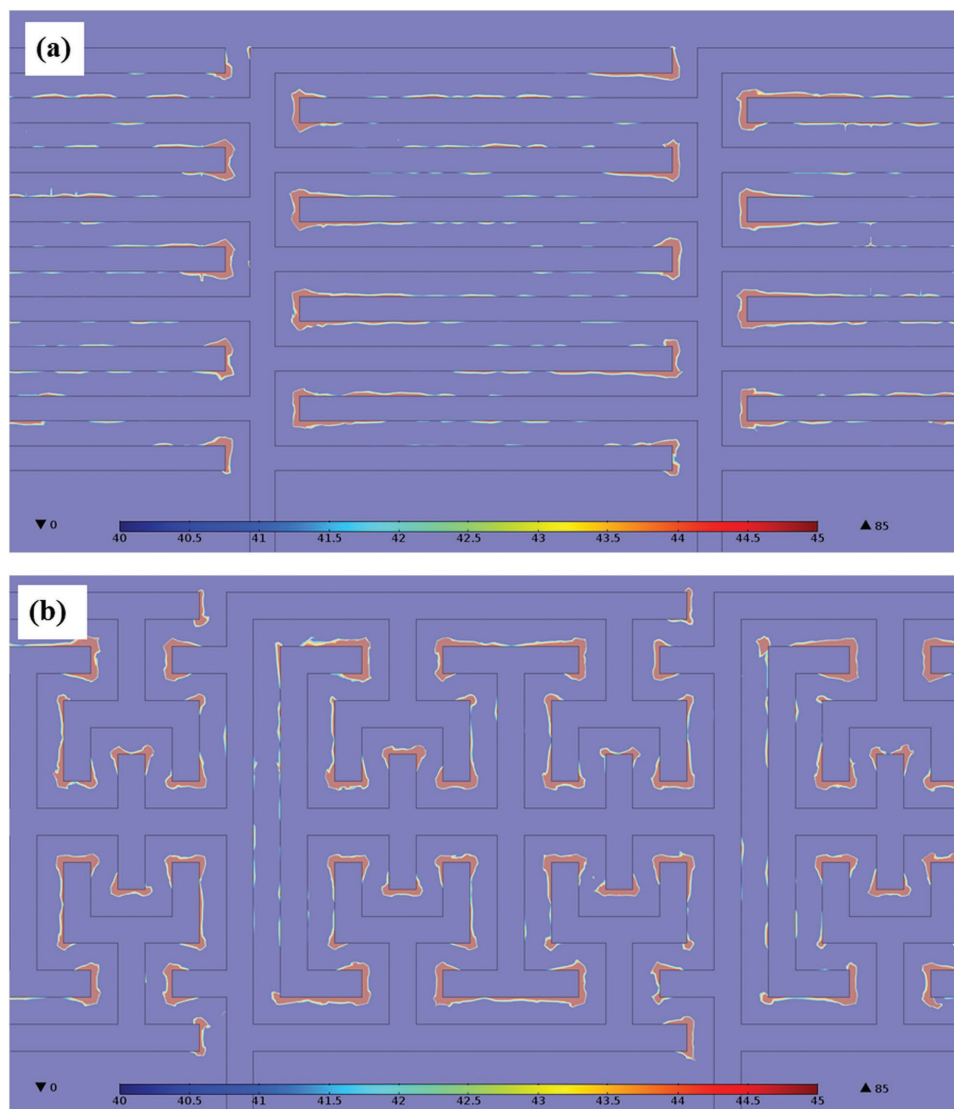
**ADVANCED
SCIENCE NEWS**
www.advancedsciencenews.com

**ADVANCED
ELECTRONIC
MATERIALS**
www.advelectronicmat.de

Figure 7. The electrical field distribution (V μm^{-1}) obtained from the COMSOL simulation tool for a) IDE and b) one of the fractal electrode designs.

in **Figure 7**a,b, respectively. Here, we used COMSOL simulation tool to simulate the electric field and extract corresponding images. It can be clearly observed from our simulations that electrical field strength increases near the sharp edges in both IDE and the fractal designs (see the red color regions and the corresponding values in the color bar given below each image). Since the number of open edges is higher in the case of fractal designs, it can be deduced that the density of the electrical lines of force increases in the case of fractal electrodes. The numbers of open edges are also different for different fractal designs, leading to variation in their capacitance values.

3. Conclusion

In summary, we have demonstrated the successful fabrication of microsupercapacitors with interdigital and fractal electrode designs. It is observed that better electrochemical performance can be achieved using fractal electrodes. Among the different electrode designs used in this study, the Moore design shows the best performance. Specifically, microsupercapacitors with the Fractal Moore electrode design exhibit a maximum areal capacitance of ≈11 mF cm^{-2} with a volumetric capacitance of ≈168 F cm^{-3}. In comparison, an areal capacitance of ≈8 mF cm^{-2} and a volumetric capacitance ≈125 F cm^{-3} were obtained in the case of IDE electrode design using identical electrode materials. About 32% improvement in the volumetric energy density is obtained using fractal Moore electrodes as compared to IDE designs, when measured at the same power density (769 mW cm^{-3}). We show that the active electrode surface area cannot alone explain the increase in capacitance of fractal electrodes. It is proposed that the increase in the total number of electrical lines of force, due to edging effects in the fractal designs, enhance electrolyte ion absorption, and improve electrochemical performance. This study shows that fractal electrode designs provide a promising approach to improving

the performance of integrated electrochemical microsupercapacitors at no extra cost.

4. Experimental Section

The μ-SCs were fabricated on glass substrates. Device fabrication starts with the cleaning of the glass substrates with acetone, isopropanol, and deionized (DI) water for 5 min each in an ultrasonication bath. A bilayer of Ti (≈20 nm)/Au (≈150 nm) was deposited on the glass before RuO_2 deposition and used as a current collector. The RuO_2 was deposited at room temperature using a 2 in. Ru target in reactive sputtering mode under argon and oxygen ambient with 80 W RF power at a deposition pressure of 3 mTorr. Different oxygen partial pressures (O_{pp}) were tried—including 0, 8, 15, 22, and 28% O_{pp}—to optimize the deposition conditions, keeping other parameters constant. The μ-SC devices were fabricated using RuO_2 deposited in 28% O_{pp}. To get an optimum thickness for the final devices, the thickness-dependent performance of the μ-SCs was studied by using interdigitated electrode design and 110, 450, 650, and 900 nm thick RuO_2 films. The μ-SC devices were patterned using a standard optical lithography and lift-off process in acetone. A 10 μm thick AZ9260 photoresist coating was used for the lithography process. It was developed in the AZ726 developer solution. The thicknesses of different films were measured by a surface profilometer (Veeco Decktak 150). Chemical composition and structural analyses of the films were performed using XPS, XRD, and Raman spectroscopy. XPS studies were carried out in a Kratos Axis Ultra DLD spectrometer equipped with a monochromatic Al Kα X-ray source (hv = 1486.6 eV) operating at 150 W, a multichannel plate, and a delay-line detector under a vacuum of 10^{-9} mbar. A Bruker D8 Discover thin-film X-ray diffractometer and a Horiba Aramis UV spectrometer were used for XRD (Cu Kα X-ray source of λ = 0.15406 nm) and Raman measurements (He-Ne laser of wavelength 633 nm). Electrochemical measurements for the μ-SC devices used in this study were performed on full-cell devices (in the two-electrode configuration). The areal and volumetric capacitances of the μ-SC devices were calculated by taking the total area and volume of the electroactive electrodes into consideration. CV, galvanostatic CD, and electrochemical-cycling stability analyses were performed in 1 M H_2SO_4 electrolyte solution using a VMP3 multichannel electrochemical workstation (Bio-Logic). The CVs were measured in a voltage window between 0 and 1.0 V at different scan rates selected from 50 to 1000 mV s^{-1}. The CDs were measured in the same voltage window under different current densities selected from 100 μA cm^{-2} to 3 mA cm^{-2}. All measurements were carried out at room temperature.

Supporting Information

Supporting Information is available from the Wiley Online Library or from the author.

Acknowledgements

Conflict of Interest

The authors declare no conflict of interest.

[1] B. Wang, M. Ahmed, B. Wood, F. Iacopi, *Appl. Phys. Lett.* **2016**, *108*, 183903.

[2] J. Li, V. Mishukova, M. Ostling, *Appl. Phys. Lett.* **2016**, *109*, 123901.

[3] Q. Jiang, N. Kurra, C. Xia, H. N. Alshareef, *Adv. Energy Mater.* **2017**, *7*, 1601257.

[4] X. Tian, M. Shi, X. Xu, M. Yan, L. Xu, A. Minhas-Khan, C. Han, L. He, L. Mai, *Adv. Mater.* **2015**, *27*, 7476.

[5] N. Kurra, B. Ahmed, Y. Gogotsi, H. N. Alshareef, *Adv. Energy Mater.* **2016**, *6*, 1601372.

[6] E. Frackowiak, F. Béguin, *Carbon* **2001**, *39*, 937.

[7] Z. Niu, L. Zhang, L. Liu, B. Zhu, H. Dong, X. Chen, *Adv. Mater.* **2013**, *25*, 4035.

[8] X. Zhang, X. Liu, S. Zeng, J. Fang, C. Men, X. Zhang, Q. Li, *Nanoscale Res. Lett.* **2017**, *12*, 165.

[9] M. Kaempgen, C. K. Chan, J. Ma, Y. Cui, G. Gruner, *Nano Lett.* **2009**, *9*, 1872.

[10] A. Soam, P. Kavle, A. Kumbhar, R. O. Dusane, *Curr. Appl. Phys.* **2017**, *17*, 314.

[11] X. C. Dong, H. Xu, X. W. Wang, Y. X. Huang, M. B. Chan-Park, H. Zhang, L. H. Wang, W. Huang, P. Chen, *ACS Nano* **2012**, *6*, 3206.

[12] C. Xu, Y. Zhao, G. Yang, F. Li, H. Li, *Chem. Commun.* **2009**, *48*, 7575.

[13] J. Y. Kim, S.-H. Lee, Y. Yan, J. Oh, K. Zhu, *RSC Adv.* **2012**, *2*, 8281.

[14] J. Zang, S.-J. Bao, C. M. Li, H. Bian, X. Cui, Q. Bao, C. Q. Sun, J. Guo, K. Lian, *J. Phys. Chem. C* **2008**, *112*, 14843.

[15] M. A. Garakani, S. Abouali, B. Zhang, Z. L. Xu, J. Huang, J. Q. Huang, E. K. Heidari, J. K. Kim. *J. Mater. Chem. A* **2015**, *3*, 17827.

[16] H. Wang, L. Zhang, X. Tan, C. M. B. Holt, B. Zahiri, B. C. Olsen, D. Mitlin, *J. Phys. Chem. C* **2011**, *115*, 17599.

[17] Q. Guan, J. Cheng, B. Wang, W. Ni, G. Gu, X. Li, L. Huang, G. Yang, F. Nie, *ACS Appl. Mater. Interfaces* **2014**, *6*, 7626.

[18] L. Nottale, J. Schneider, *J. Math. Phys.* **1984**, *25*, 1296.

[19] B. B. Mandelbrot, *Les Objects Fractals*, Flammarion, Paris, **1975**.

[20] H. O. Peitgen, H. Jürgens, D. Saupe, *Chaos and Fractals*, Springer-Verlag, New York, **1990**.

[21] A. M. Elshurafa, A. G. Radwan, A. Emira, K. N. Salama, *IEEE J. Microelectromech. Syst.* **2012**, *21*, 10.

[22] B. Mandelbrot, *Proc. Natl. Acad. Sci. USA* **1975**, *72*, 3825.

[23] L. Golestanirad, C. Pollo, S. J. Graham, presented at 35th Annual Int. Conf. IEEE EMBS Osaka, Japan, July, **2013**.

[24] H. Samavati, A. Hajimiri, A. R. Shahani, G. N. Nasserbakht, T. H. Lee, *IEEE J. Solid-State Circuits* **1998**, *33*, 2035.

[25] F. Afshinmanesh, A. G. Curto, K. M. Milaninia, N. F. V. Hulst, M. L. Brongersma, *Nano Lett.* **2014**, *14*, 5068.

[26] S. D. Zuani, T. Reindl, M. Rommel, B. Gompf, A. Berrier, M. Dressel, *ACS Photonics* **2015**, *2*, 1719.

[27] Y. Mashraei, S. Sivashankar, U. Buttner, K. N. Salama, *IEEE Sens. J.* **2016**, *16*, 8775.

[28] J. A. Fan, W. H. Yeo, Y. Su, Y. Hattori, W. Lee, S. Y. Jung, Y. Zhang, Z. Liu, H. Cheng, L. Falgout, M. Bajema, T. Coleman, D. Gregoire, R. J. Larsen, Y. Huang, J. A. Rogers, *Nat. Commun.* **2014**, *5*, 3266.

[29] A. M. Elshurafa, P. H. Ho, A. G. Radwan, M. H. Ouda, K. N. Salama, *IET Micro Nano Lett.* **2012**, *7*, 965.

[30] B. Y. Park, R. Zaouk, C. Wang, M. J. Madou, *J. Electrochem. Soc.* **2007**, *154*, P1.

[31] R. Aparicio, A. Hajimiri, *IEEE J. Solid-State Circuits* **2002**, *37*, 384.

[32] D. Hilbert, *Math. Ann.* **1891**, *38*, 459.

[33] G. A. Bliss, *Bull. Am. Math. Soc.* **1934**, *40*, 501.

[34] G. Peano, *Math. Ann.* **1890**, *36*, 157.

[35] Y. L. Kim, H. A. Choi, N. S. Lee, B. Son, H. J. Kim, J. M. Baik, Y. Lee, C. Lee, M. H. Kim, *Phys. Chem. Chem. Phys.* **2015**, *17*, 7435.

[36] Y. L. Chueh, C. H. Hsieh, M. T. Chang, L. J. Chou, C. S. Lao, J. H. Song, J. Y. Gan, Z. L Wang, *Adv. Mater.* **2007**, *19*, 143.

[37] K. H. Chang, C. C. Hu, *Appl. Phys. Lett.* **2006**, *88*, 193102.

[38] W. Dmowski, T. Egami, K. E. S. Lyons, C. T. Love, D. R. Rolison, *J. Phys. Chem. B* **2002**, *106*, 12677.

[39] A. V. Korotcov, Y.-S. Huang, K.-K. Tiong, D. S. Tsai, *J. Raman Spectrosc.* **2007**, *38*, 737.

[40] S. Y. Mar, C. S. Chen, Y. S. Huang, K. K. Tiong, *Appl. Surf. Sci.* **1995**, *90*, 497.

[41] D. Rochefort, P. Dabo, D. Guay, P. M. A. Sherwood, *Electrochim. Acta* **2003**, *48*, 4245.

[42] C. Mun, J. J. Ehrhardt, J. Lambert, C. Madi, *Appl. Surf. Sci.* **2007**, *253*, 7613.

[43] M. A. Ernst, W. G. Sloof, *Surf. Interface Anal.* **2008**, *40*, 334.

[44] Y. J. Kim, Y. Gao, S. A. Chambers, *Appl. Surf. Sci.* **1997**, *120*, 250.

[45] D. J. Morgan, *Surf. Interface Anal.* **2015**, *47*, 1072.

[46] S. Barison, D. Barreca, S. Daolio, M. Fabrizio, E. Tondello, *J. Mater. Chem.* **2002**, *12*, 1511.

[47] P. Simon, Y. Gogotsi, *Nat. Mater.* **2008**, *7*, 845.

[48] J. W. Long, K. E. Swider, C. I. Merzbacher, D. R. Rolison, *Langmuir* **1999**, *15*, 780.

[49] W. Wang, S. Guo, I. Lee, K. Ahmed, J. Zhong, Z. Favors, F. Zaera, M. Ozkan, C. S. Ozkan, *Sci. Rep.* **2014**, *4*, 4452.

[50] A. Ferris, S. Garbarino, D. Guay, D. Pech, *Adv. Mater.* **2015**, *27*, 6625.

[51] M. Ahmed, M. Khawaja, M. Notarianni, B. Wang, D. Goding, B. Gupta, J. J. Boeckl, A. Takshi, N. Motta, S. E. Saddow, F. Iacopi, *Nanotechnology* **2015**, *26*, 434005.

[52] B. G. Choi, M. H. Yang, W. H. Hong, J. W. Choi, Y. S. Huh, *ACS Nano* **2012**, *6*, 4020.

[53] B. B. Mandelbrot, R. Pignoni, *The Fractal Geometry of Nature*, Vol. *1*, WH Freeman, New York, **1983**.